Experiment and CFD Simulation to Investigate Two Kinds of Condensation in Ceramic Nanoporous Membranes

Tianwen Zhang *, Handuo Zhang , Ruilin Wang , Shengyue Huang , Shanna Wang

Posted Date: 31 March 2026

doi: 10.20944/preprints202603.2439.v1

Keywords: ceramic nanoporous membrane; capillary condensation (CCD); experiment; CFD simulation; heat and mass transfer

 doi:10.20944/preprints202603.2439.v1

Article

Experiment and CFD Simulation to Investigate Two Kinds of Condensation in Ceramic Nanoporous Membranes

Tianwen Zhang [1,*], Handuo Zhang [2] and Ruilin Wang [1],Shengyue Huang [1],Shanna Wang [3]

[1] School of Energy and Power, Changchun Institute of Technology, Chang Chun 130012, China

[2] Xi'An Jiaotong University, Xi'An 710049, China

[3] Jilin Justice Officer Academy, Chang Chun 130216, China

* Correspondence: 15666239336@163.com

Abstract

A nanoporous tubular ceramic membrane (TCM) was developed to recover water vapor and significant latent heat from flue gas, in order to conserve water and reduce the acid dew point. Experimental and numerical investigations were conducted on both normal condensation (NCD) and capillary condensation (CCD) by integrating a horizontal TCM into a membrane module. Using User-Defined Functions (UDFs) in ANSYS Fluent 14.5, source terms were implemented in the governing equations to elucidate the mechanisms of NCD and CCD, as well as the effects of inertia force (F_i) on heat and mass transfer. Simulations were performed across various parameters, including feed gas inlet velocity (U_{in}), mass fraction of non-condensable gas (W_{con}), cooling water inlet temperature (T_{cool}), and time steps (t). The relative error between experimental and numerical results was found to be less than 1.14%. The results indicate that the thermal performance contribution of NCD is more significant than that of CCD. NCD occurs significantly throughout the TCM flow channel, whereas CCD primarily takes place in the downstream region of the TCM (approximately x > 500 mm). Furthermore, U_{in}, W_{con}, and T_{cool} were found to have a significant influence on the heat and mass transfer characteristics.

Keywords: ceramic nanoporous membrane; capillary condensation (CCD); experiment; CFD simulation; heat and mass transfer

1. Introduction

Ceramic membrane tubes are widely utilized as porous media in various industrial applications, such as thermal power plants, due to their exceptional capability to extract and recover water vapor from flue gas[1]. As flue gas flows through the ceramic membrane tube, water vapor condenses due to changes in temperature or equilibrium pressure. The condensate permeates through the nanopores of the membrane wall and is removed by the cooling water flow, accompanied by significant latent heat transfer.

Recently, several researchers have investigated the heat transfer and water recovery performance of these membranes. In 2016, Chen et al.[2] experimentally examined the water recovery rate of a 50 nm pore-sized ceramic membrane tube under varying operational conditions, including cooling water temperature and flow rate. Their results indicated that the water recovery rate could reach a maximum of 2.5 kg/m²·h. Similarly, Hu et al.[3] compared the thermal characteristics of a 100 nm ceramic membrane tube with a fluorine plastic tube of identical dimensions. They reported that the heat transfer efficiency of the ceramic membrane tube was 1.3 to 2 times higher than that of the plastic tube under the same experimental conditions.

As a porous medium, the ceramic membrane tube facilitates two distinct condensation processes. The first, known as capillary condensation (CCD), occurs due to the alteration of the

 doi:10.20944/preprints202603.2439.v1

equilibrium pressure of water vapor within the membrane pores relative to the corresponding saturation pressure[4]. The second, termed normal condensation (NCD), results from forced convection heat transfer between the water vapor and the membrane surface driven by the temperature gradient across them. Due to the contribution of CCD, the condensation rate of ceramic membrane tubes[3,4] is typically 1.7 to 3 times greater than that of traditional condensing materials; consequently, CCD behavior has been extensively studied theoretically. Using the Young–Laplace equation, Uchytil[5] determined the critical pressure difference in the CCD process and correlated it with the mass transfer coefficient. Loimer[6] provided a more detailed analysis of the CCD mechanism, concluding that instantaneous pressure fluctuations were the primary factor affecting CCD. Furthermore, both the Joule–Thomson coefficient and the convection heat transfer coefficient were found to increase significantly with the assistance of CCD.

Numerous researchers have also conducted experimental and theoretical investigations into normal condensation (NCD)[7–10]. Fu et al.[7] studied the relationship between vapor content and latent heat flux during the condensation process, finding that a nitrogen mass fraction of approximately 5% led to a 13.7% decrease in the condensation rate. Bao et al.[8] simultaneously evaluated condensation heat transfer and water recovery performance. They observed that the condensation mass flux (ranging from 8 to 15.3 kg/m²·h) improved significantly with an increase in vapor mass fraction (from 0.12 to 0.2) but decreased as the nitrogen mass fraction increased (from 0.8 to 0.9). These findings suggest that the normal condensation process is significantly hindered by the presence of non-condensable gases.

In recent years, Computational Fluid Dynamics (CFD) has become a popular approach for studying the influence of non-condensable gases on NCD[11–14], owing to its time-saving potential and ability to provide detailed insights. Huang et al.[11] defined the resistance of non-condensable gas to heat transfer using a new dimensionless number: the suction effect. The authors reported that non-condensable gas accumulates near the wall surface, forming a boundary layer that resists vapor penetration. Additionally, the presence of non-condensable gas reduces the partial pressure of water vapor, thereby retarding the condensation process. Further studies have deeply investigated heat and mass transfer processes in the presence of non-condensable gas[7,11–18], developing relevant experimental correlations. Fu et al.[7] investigated variations in the diffusion coefficient using the analogy method, showing that the diffusion coefficient declines with increasing nitrogen mass fraction. Based on Knudsen's theory, Caruso et al.[12] recently found that the increase in the Sherwood number was more pronounced due to the suction effect of non-condensable gas. Yi et al.[13] performed experiments focusing on non-condensable gas to evaluate heat flux variations. Numerical modeling of the mass transfer process has also been conducted; for instance, Behrang et al.[14] proposed a permeability model based on gas kinetic theory coupled with fractal techniques. They concluded that the condensation process leads to a decrease in permeability, attributing this trend to the remarkable suction effect of non-condensable gas.

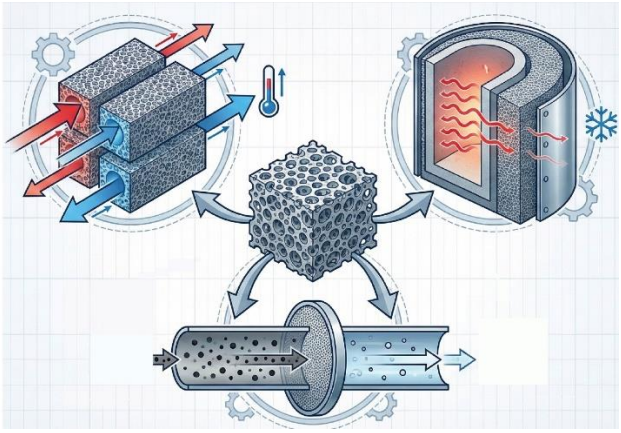

Figure 1. Industrial applications of porous media.

 doi:10.20944/preprints202603.2439.v1

Despite the extensive recent efforts in CFD-experimental studies on membrane condensation[19–22], the detailed transient mechanisms governing the multi-stage condensation process—particularly the distinction of two-phase flow characteristics between normal condensation (NCD) and capillary condensation (CCD)—remain poorly understood. To bridge this gap, this study aims to develop a macroscopic heat and mass transfer mathematical model containing heat source term expressions for different condensation behaviors (NCD and CCD). We address this gap through a combined numerical and experimental approach. Numerically, source terms representing the suction effect of non-condensable gas and inertia forces[23,24] were modeled using User-Defined Functions (UDFs) in Fluent 14.5, with fluid parameters derived from NIST 14.0. The significant novelty of this work lies in revealing the multi-level condensing mechanism induced by porous structures and thermal gradients within membrane walls. This study provides new physical insights into the underlying mechanisms driving the nonlinear and heterogeneous heat and mass transfer behaviors during condensation within porous media.

The distinction between NCD and CCD was investigated numerically and experimentally. It was found that the condensing behavior present within porous material is complex, with NCD and CCD forming synchronously once triggering conditions are met, e.g., when the relative partial pressure of water vapor is saturated. Additionally, the disparate onset conditions (e.g., wall temperature, inlet velocity, and fraction of non-condensable gas) for the two condensation behaviors induce irregular and nonlinear condensation heat and mass transfer within the porous ceramic membrane. The investigation focused on three key aspects: (1) the effects of feed gas inlet velocity on both condensation types; (2) the influence of non-condensable gas mass fraction; and (3) the thermal performance of the TCM under NCD conditions with varying cooling temperatures. The aim was to investigate the thermal performance on the membrane surface experimentally and analyze permeating behavior and capillary condensing heat-transfer characteristics within porous zones using CFD.

2. Experimental and Numerical Methods

2.1. Heat and Mass Transfer Mechanism

The experimental module consists of a horizontal, nanoporous tubular ceramic membrane (TCM) and digital gauges. The basic parameters of the TCM are obtained from the manufacturer's specification. The inner diameter is *0.012m*, the thickness is *0.0015m*, and the length is *0.6m*; the other performance parameters are listed in *Table 1*.

The vapor of feed gas may condense into liquid while flowing in two ways, namely, normal condensation (NCD) and capillary condensation (CCD). NCD occurs when the water vapor of feed gas condenses into liquid because of the heat transfer process between the feed gas and the membrane's surface are cooled by cooling water, and then the condensate permeates through the TCM wall due to trans-membrane pressure difference. CCD occurs when the feed gas gets into the nanopores: the saturated pressure of water vapor varies sharply and instantaneously, and the water vapor condenses into liquid. The schematic of flow in the TCM is shown in *Figure 2*.

Phase-changing heat transfer performance on membrane can be controlled not only by condensing mode but also by thermal resistance caused by heterogeneous phase distribution. As depicted in *Figure 2*, three different types of thermal resistance occur near the wall, namely, membrane thermal resistance, droplet thermal resistance, and film thermal resistance. Conversely, thermal resistance during the film-wise condensation process only consists of membrane thermal resistance and condensate film thermal resistance. This can be attributed to the fact that a multi-level condensation process appears within the porous material, and heterogeneous condensate forms accumulate near porous zones.

 doi:10.20944/preprints202603.2439.v1

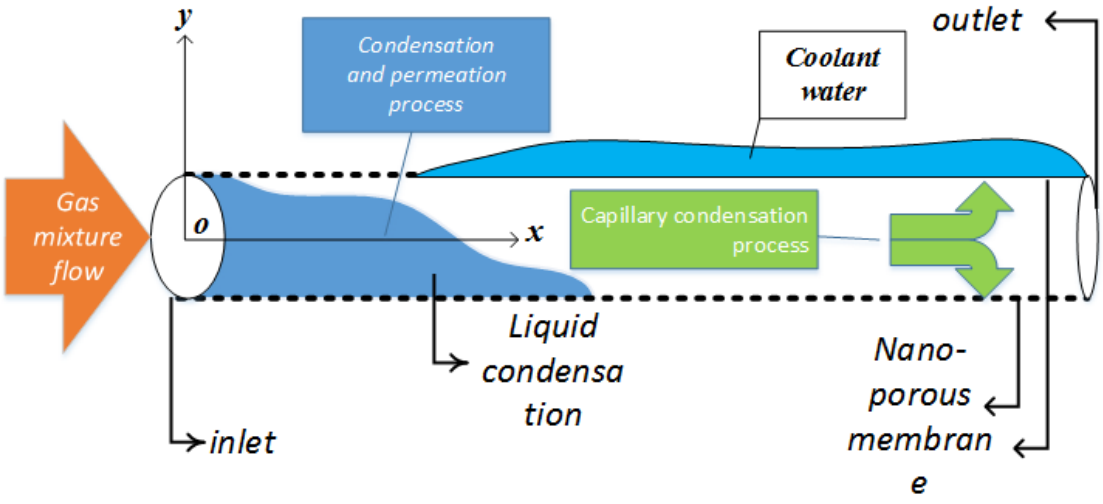

Figure 2. Configuration and theory of the ceramic tube with nanoporous membrane.

Because the physical model was axisymmetric, a two-dimensional axisymmetric model and structured grids were used in this study, and we selected the top half of the TCM as the simulation domain. The mass and heat transfer from the gas mixture to the coolant was implemented into *Fluent14.5* by adding source terms to the cells adjacent to the wall. To ensure the accuracy of our results, the near-wall grids were refined. This research focuses on the influences of condensing behaviors on thermal and mass-transfer characteristics within the ceramic membrane, rather than the wetting characteristics (e.g. contact angle and pore-size distribution) or other negligible conditions.

The overall ceramic membrane features a structural gradient macroscopically, and the characteristic pore size distribution within the specific local computational domain is relatively narrow. Therefore, assuming a uniform pore size for the local pore-scale simulation is a reasonable simplification. In addition, a constant contact angle is assumed because the temperature variation across the membrane interface under the current operating conditions is relatively small (less than *0.7 K*). Within this moderate temperature range, the temperature-induced variations in fluid surface tension and local solid–liquid wettability are negligible compared to the dominant capillary and viscous forces. Neglecting thermal radiation, it can be concluded that the operating temperature of the membrane condensation process is relatively low (ranging from *293* to *362.17 K*). Under these conditions, the total heat flux is overwhelmingly dominated by the latent heat of phase change and convective heat transfer. The radiative heat flux is orders of magnitude smaller and can thus be safely omitted without affecting the accuracy of the thermal transport analysis.

For the purpose of maintaining accuracy and computational node-saving, several reasonable assumptions are presented before simulation initialization as a similar numerical model[17]**:**

- Thermal radiation has a negligible effect on convective heat transfer.
- Condensation only occurs in the near-wall region of the TCM (the wall surface of the TCM).
- There is a unique contact angle throughout the whole TCM's surface[22]; that is, the surface hydrophilicity of the TCM is uniform. Additionally, the pores within the TCM wall are all the same size.

While the aforementioned assumptions are necessary to maintain computational tractability, it is important to acknowledge how deviations from these idealized conditions might affect the predicted results. The real porous media inherently possess a pore size distribution rather than a strictly uniform pore size. A localized variation in pore size would induce non-uniform capillary pressure fields, potentially leading to preferential liquid flow paths (fingering effects) and localized liquid pooling. This deviation implies that our idealized model might slightly overestimate the overall condensation heat transfer coefficient, as localized flooding in real non-uniform pores would add additional thermal resistance.

 doi:10.20944/preprints202603.2439.v1

A real condensing surface exhibits contact angle hysteresis (differences between advancing and receding contact angles) rather than a constant static contact angle. The presence of hysteresis would increase the adhesion force (pinning effect) on the liquid–vapor interface, delaying liquid removal from the porous structure. Consequently, the actual liquid film thickness might be greater than predicted, meaning that our current model likely yields a conservative estimate of thermal resistance.

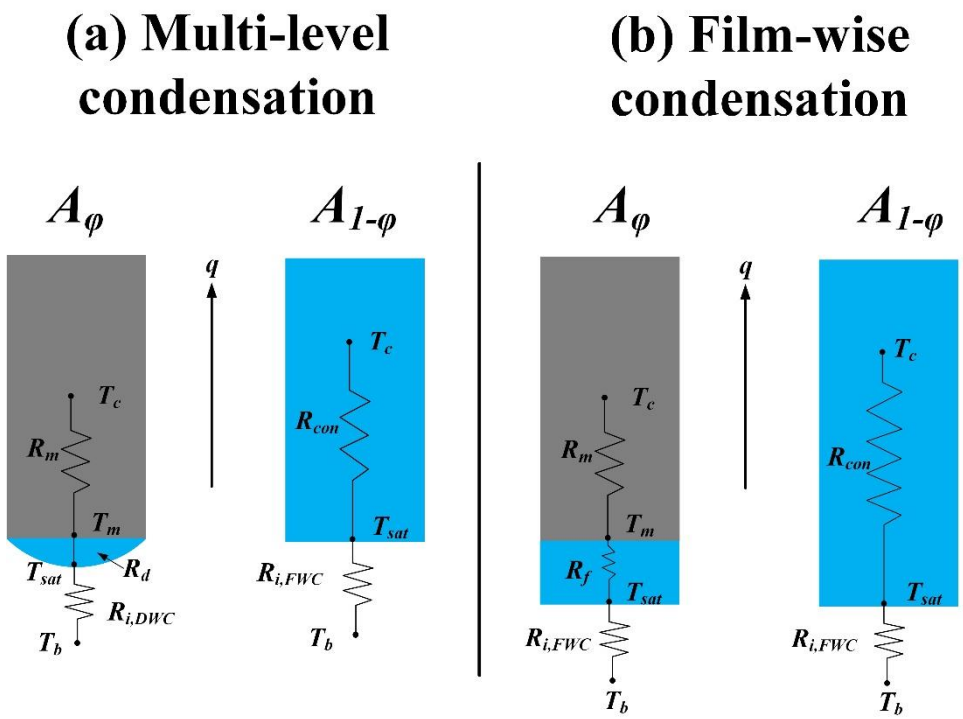

Figure 3. Introduction of thermal resistance on multi-level condensation and film-wise condensation process.

Importantly, if thermal radiation were incorporated, it would act as a parallel heat transfer pathway, resulting in a marginal increase in the total predicted heat flux. However, given the low operating temperatures, this underestimation of the total heat flux is considered physically negligible.

Table 1. Basic parameters of the TCM.

Length of tube (mm)	Radius of tube (mm)	Porosity of membrane	Tortuosity of membrane	Thickness of membrane (mm)	Contact angle (º)	Surface tension (N/m)	Diameter of pore in membrane (nm)
600	6.02	40%	2.8	1.5	33.7	0.0718	20

2.2. Experimental Method and Tools

The sketch of experimental configuration is presented in *Figure 4*, in order to simulate the actual gas in the gas-fired power plant[19], and the nitrogen and water vapor are chosen and mixed in the gas mixing tank (*NO.4*) equipment before getting into the membrane module. In order to achieve higher mixing efficiency, the feed gas is introduced into the membrane module in the *1, 2* gas buffer tank (*NO.1, 2*) or the humidifier (*NO.3*) and is heated into fixed temperature in the thermostatic water tank (*NO.5*). The mass flow of feed gas and cooling water are controlled by a mass flow controller and a pump, respectively, and the cooling water's temperature and pressure at the inlet and outlet of the membrane module are measured by digital temperature and vacuum gauges. The electric heater (*NO.7*) equipment plays a key role in the experimental configuration. In order to investigate the CCD, the electric heater is used to heat the cooling water so that the cooling temperature is always higher

 doi:10.20944/preprints202603.2439.v1

than the saturated temperature at fixed conditions. Without using the electric heater (*NO.7*), however, the cooling temperature is always lower than the saturated temperature, and we use the cooling water to investigate the NCD directly. The mass measurement of the drying pipe (*NO.6*) is used to obtain the values of recovery water mass. The mass difference measured by two water tanks can also verify the mass flux of recovery water. The measurement is carried out continuously every *10* minutes, and data is collected after *50* minutes.

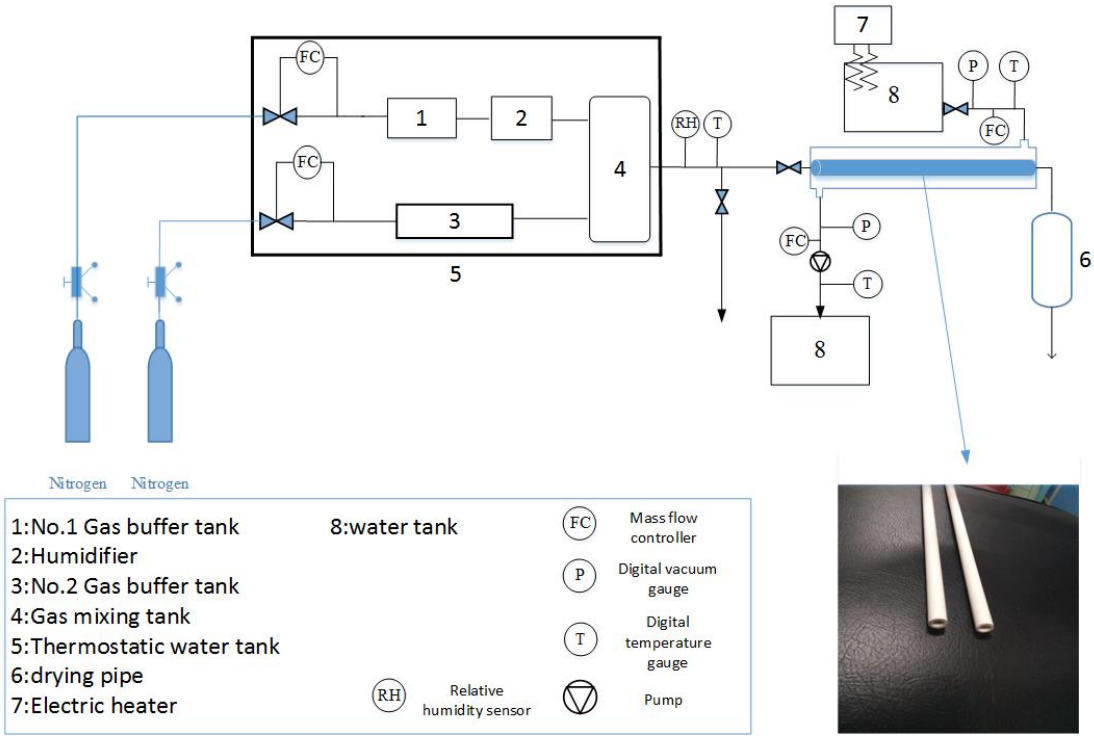

Figure 4. Schematic diagram of experimental configuration.

2.3. Equations

NCD and CCD models are implemented into the *FLUENT14.5* code using different numerical models of diffusion mass flux, and the basic parameters of feed gas and liquid condensation are referenced from the commercial software *NIST 14.0*.

Table 2. Distinction between the condensing behaviors.

	Normal Condensation	**Capillary Condensation**
Scale	Macroscopic	Mesoscopic
Forming mechanism	Dalton's Law of Partial Pressures	Laplace Law
Forming zone	Wetting surface on membrane wall	Porous zone within membrane

According to the variation range of Knudsen numbers[3], both the feed gas and condensate get through the pores in the TCM as Knudsen flow and viscous flow during the CCD process, while only viscous flow exists during NCD. The distinction between NCD and CCD is presented in *Table 2*, and a schematic diagram of the flow in the TCM with the relevant symbols is depicted in *Figure 5*.

 doi:10.20944/preprints202603.2439.v1

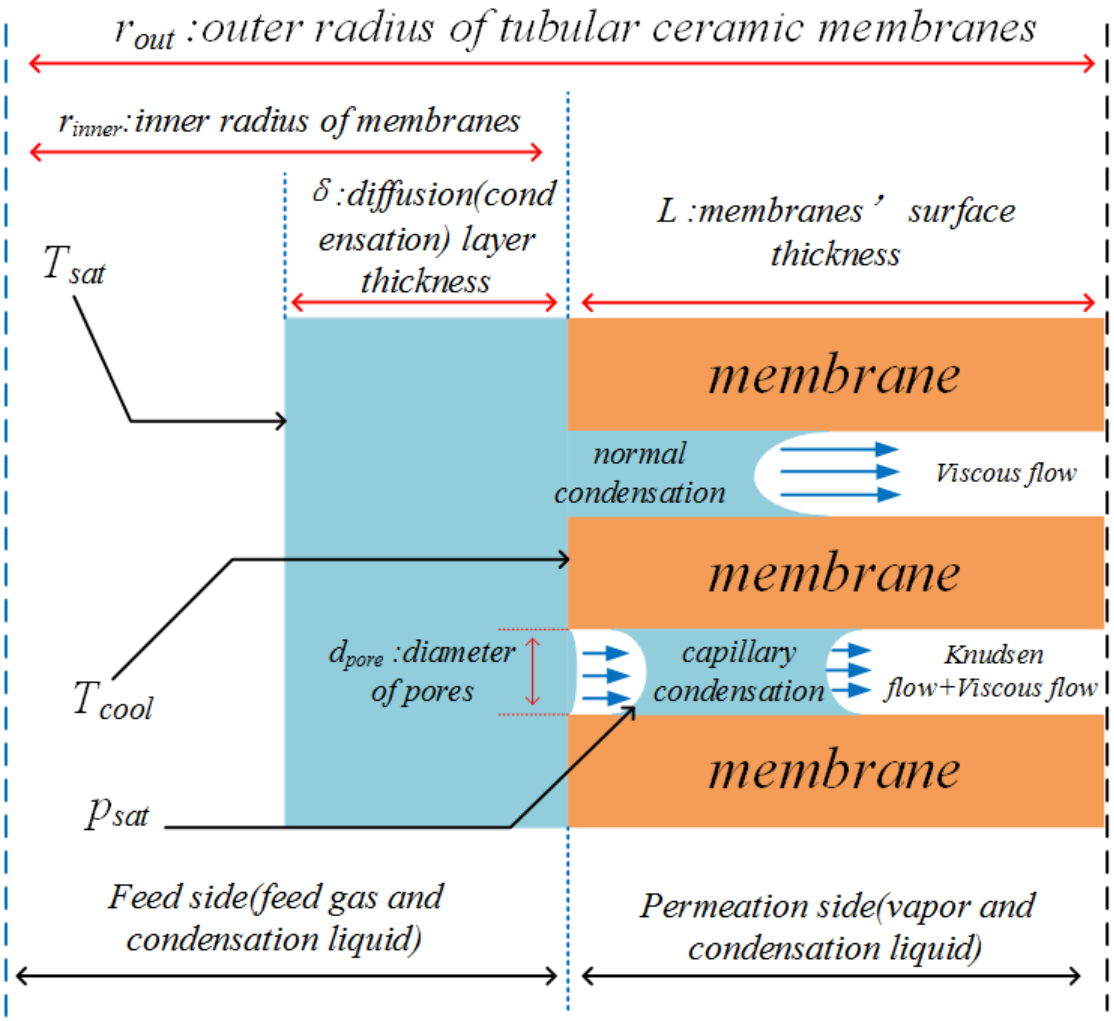

Figure 5. Schematic diagram of experimental configuration.

The Knudsen number is modeled as[3]:

$$Kn = \frac{\overline{\lambda}}{L} = \frac{k_B T}{\sqrt{2}\pi p_{pore} d_0^{\,2} \delta} \qquad (1)$$

where k_B, T, p_{pore}, d_0, and δ represent the Boltzmann number, the average temperature, the average pressure in the pore region, the molecular diameter, and the thickness of the membrane, respectively. The Boltzmann number[13] is 1.38×10^{-23}, and the Knudsen number changes from 1.23×10^{-11} to 1.28×10^{-11} when the bulk temperature of feed gas increases from $362.17K$ to $373K$. According to A.Berang[14], the pores of TCM are regarded as a slip flow regime. We assume that if the water vapor temperature (T_{vap}) is higher than the saturated temperature (T_{sat}), the feed gas will enter the pores of the TCM, and capillary condensation will subsequently occur.

Consequently, the diffusion mass flux (J) through the pores of the TCM is simply regarded as the sum of viscous flow and Knudsen flow:

$$J = J_{vis} + J_{Kn} = -(\frac{k_0 p}{\mu} + D_b)\frac{\nabla p}{RT}\frac{1}{A_{pore}} \qquad (2)$$

where k_0, D_b, μ ,M_b, and A_{pore} represent the permeability coefficient, the diffusion coefficient of feed gas, dynamic viscosity, the molar weight of feed gas, and the area of pores within the membrane, respectively. k_0 and D_{eff} are expressed as:

 doi:10.20944/preprints202603.2439.v1

$$k_0 = \frac{r_{pore}^{\ 2}}{45}\frac{\psi^3}{(1-\phi)^2} \tag{3}$$

$$\frac{1}{D_{eff}} = \frac{1-W_{vap}}{D_b} + \frac{W_{vap}}{D_{con}} \tag{4}$$

where r_{pore}, ψ, φ, D_{con}, and W_{vap} represent the radius of pores, porosity, the suction effect coefficient, the diffusive coefficient of the condensate, and the mass fraction of water vapor, respectively. D_b and D_{con} are calculated as follows:

$$D_b = \frac{2r_{pore}}{3}\sqrt{\frac{8k_BT}{\pi M_b}} \tag{5}$$

$$D_{con} = \frac{1.883\times10^{-22}T^{1.5}}{p\sigma^2}\left(\frac{1}{M_b}+\frac{1}{M_{vap}}\right)^{0.5} \tag{6}$$

where M_b and M_{vap} represent the mole weight of feed gas and water vapor, respectively. σ represents the characteristic size of the gas mixture (i.e. the effective collision diameter of the molecules in the mixture), and its value equals *30nm*.

For NCD, the steady-state diffusion equation along the y-coordinate (distance from the middle of the membrane to the wall surface) can be calculated using *Eq(7), (8), (9):*

$$m_{vap} = m_b W_{vap} - \rho_b D_{eff}\frac{\partial W_{vap}}{\partial y} \tag{7}$$

$$m_{non} = m_b W_{non} - \rho_b D_{eff}\frac{\partial W_{non}}{\partial y} \tag{8}$$

$$m_b = m_{vap} + m_{non} \tag{9}$$

where m_b, m_{vap}, and W_{vap} represent the mass flux of the feed gas, mass flux, and the mass fraction of water vapor. We assume that the condensation interface is impermeable, and the non-condensable gas mass flux in the condensation interface should be zero:

$$0 = m_b W_{non} - \rho_b D_{eff}\frac{\partial W_{non}}{\partial y} \tag{10}$$

With the assumption[14] that the diffusive coefficient of gas mixture D_b is a function of the *y-coordinate* and the value of ρ_b can be obtained from *NIST14.0*, *Eq(10)* can be integrated between the gas mixture and condensation interface:

$$\int_{w_{vap,0}}^{w_{vap}}\frac{d(1-w_{vap})}{(1-w_{vap})} = \frac{m_b}{\rho_b D_{eff}}\int_0^{\delta} dy \tag{11}$$

where $y=\delta$ represents the diffusion layer thickness.

$$m_{vap} = m_b W_{vap} = \frac{\rho_b D_{eff} W_{vap}}{\delta}\ln\left(\frac{1-W_{vap}}{1-W_{vap,0}}\right) \tag{12}$$

 doi:10.20944/preprints202603.2439.v1

In this study, the inertia effects[19–21] on heat convective transfer are evaluated[19], taking the thermophoretic force (F_{th}) into consideration.

$$F_{th} = \frac{-36\mu_b^{\,2} C_s(\lambda_b + C_t + Kn)}{\rho_b d_m^{\,2}(1 + C_m Kn)(1 + 2\lambda/\lambda_b + 2C_t Kn)} \frac{\nabla T}{T} \tag{13}$$

where ρ_b represents the density of the feed gas mixture; its values are listed in *Table 3*. According to the research of I.Z.Famileh[20], C_m,C_t, and C_s are set as *1.14*, *2.18*, and *1.17*, respectively.

NCD occurs outside the membrane if T_{vap} is lower than T_{sat}. CCD occurs in the pores of membranes, and not only is the T_{vap} higher than T_{sat}, but also the vapor partial pressure (p_{vap}) is lower than the saturated pressure (p_{sat}) in the nanopores. Based on the conservation of mass, the general steady-state equation of continuity is given by:

$$\nabla(\rho V) = S_{mass} \tag{14}$$

where S_{mass} in the CCD and NCD are expressed as *Eq(15)*, *(16)*, respectively:

$$S_{mass} = -\left(\frac{k_0 p}{\mu} + M_b D_{eff}\right) \frac{\nabla p}{RT} \frac{1}{A_{pore}} \quad \text{if } T_{vap} > T_{sat},\ p_{vap} < p_{sat} \tag{15}$$

$$S_{mass} = -\frac{\rho_b D_{eff} W_{vap}}{\delta} \ln\left(\frac{1 - W_{vap}}{1 - W_{vap,0}}\right) \frac{A_{cell}}{v'_{cell}} \quad \text{if } T_{vap} < T_{sat} \tag{16}$$

where A_{cell} and v_{cell}' represent the area and volume of cells in the near-wall region, respectively. The steady-state species transport equation for the prediction of the variation in water vapor mass fraction is given as:

$$\nabla(\rho V W_{vap}) = \nabla J + S_{species} \tag{17}$$

$$J = \rho_{vap} D_{eff} \nabla W_{vap} \tag{18}$$

$$S_{species} = -W_{vap}\left(\frac{k_0 p}{\mu} + M_b D_{eff}\right) \frac{\nabla p}{RT} \frac{1}{A_{pore}} \quad \text{if } T_{vap} > T_{sat},\ p_{vap} < p_{sat} \tag{19}$$

$$S_{species} = -W_{vap}^2 \frac{\rho_b D_{eff}}{\delta} \ln\left(\frac{1 - W_{vap}}{1 - W_{vap,0}}\right) \frac{A_{cell}}{v'_{cell}} \quad \text{if } T_{vap} < T_{sat} \tag{20}$$

The steady-state momentum conservation equation is expressed as:

$$\nabla(\rho V V) = -\nabla p + \mu \nabla^2 V + F_{th} \tag{21}$$

The steady-state energy conservation equation is expressed as:

$$\nabla(\rho E + P)V = \nabla(\lambda \nabla T) + S_{enr} \tag{22}$$

$$S_{enr} = -\gamma\left(\frac{k_0 p}{\mu} + M_b D_{eff}\right) \frac{\nabla p}{RT} \frac{1}{A_{pore}} \quad \text{if } T_{vap} > T_{sat},\ p_{vap} < p_{sat} \tag{23}$$

$$S_{enr} = -\gamma \frac{\rho_g D_{eff} W_{vap}}{\delta} \ln\left(\frac{1 - W_{vap}}{1 - W_{vap,0}}\right) \frac{A_{cell}}{v'_{cell}} \quad \text{if } T_{vap} < T_{sat} \tag{24}$$

 doi:10.20944/preprints202603.2439.v1

where γ represents the latent heat; the values of γ are obtained from *NIST 14.0*. For a parameter R that is not directly measured but can be calculated using directly measured quantities (x_1, x_2, …, x_i), i.e., $R = f(x_1, x_2, \ldots, x_i)$, the uncertainty of R can be represented using the error propagation equation:

$$\Delta R = \sqrt{(\frac{\partial R}{\partial x_1}\delta x_1)^2 + (\frac{\partial R}{\partial x_2}\delta x_2)^2 + \ldots + (\frac{\partial R}{\partial x_i}\delta x_i)^2} \quad (25)$$

The processes of normal condensation, capillary condensation, and inertia effect on the thermal characteristics in the feed gas can be incorporated into the flow calculations via a User-Defined Function (*UDF*), which applies a customized source term in cells directly adjacent to the condensing walls. The source terms of governing equations are listed in *Table 3*.

Table 3. Source terms of equations.

Source term name	Expression
Continuity equation source term	$S_{mass} = -(\frac{k_0 p}{\mu} + M_b D_{eff})\frac{\nabla p}{RT}\frac{1}{A_{pore}}$ (if $T_{vap}>T_{sat}$, $p_{vap}<p_{sat}$)
	$S_{mass} = -\frac{\rho_g D_{eff} W_{vap}}{\delta}\ln(\frac{1-W_{vap}}{1-W_{vap,0}})\frac{A_{cell}}{v'_{cell}}$ (if $T_{vap}<T_{sat}$)
Species of vapor equation source term	$S_{species} = -W_{vap}(\frac{k_0 p}{\mu} + M_b D_{eff})\frac{\nabla p}{RT}\frac{1}{A_{pore}}$ (if $T_{vap}>T_{sat}$, $p_{vap}<p_{sat}$)
	$S_{species} = -W_{vap}^2\frac{\rho_g D_{eff}}{\delta}\ln(\frac{1-W_{vap}}{1-W_{vap,0}})\frac{A_{cell}}{v'_{cell}}$ (if $T_{vap}<T_{sat}$)
Energy conservation equation source term	$S_{enr} = -\gamma(\frac{k_0 p}{\mu} + M_b D_{eff})\frac{\nabla p}{RT}\frac{1}{A_{pore}}$ (if $T_{vap}>T_{sat}$, $p_{vap}<p_{sat}$)
	$S_{enr} = -\gamma\frac{\rho_g D_{eff} W_{vap}}{\delta}\ln(\frac{1-W_{vap}}{1-W_{vap,0}})\frac{A_{cell}}{v'_{cell}}$ (if $T_{vap}<T_{sat}$)
Momentum conservation equation source term	$S_{mom} = F_{th}$

2.4. Simulation Settings

A finite volume method is employed by solving the governing equations using *Fluent14.5*. The *SIMPLEC* scheme is appropriate when the Reynolds number is small, and we choose it for pressure treatment in this study. For the purpose of guaranteeing the second-order accuracy of the solution, second-order upwind schemes are selected to solve the governing equations. Because we built a structured grid in this paper, the *QUICK* discrete scheme was applied to momentum and energy equations. Moreover, the Reynolds number in this study was always lower than *1200*, and the flow model selected was the laminar model. The simulation material was a gas mixture, consisting of nitrogen and water vapor. The species equation model was used to investigate the variation in vapor mass fraction.

A user-defined function (*UDF*) was utilized to solve the source terms in the energy conservation and continuity equations. The mass and energy source terms were implemented using the "*DEFINE_SOURCE*" macro. To prevent unphysical mass creation, the condensation source terms are conditionally activated at the fluid–solid interfaces within the porous structure based on local cell variables. Specifically, an if-statement in the UDF continuously checks the local temperature and vapor volume fraction. The condensation source is strictly activated only when the local temperature

 doi:10.20944/preprints202603.2439.v1

drops below the saturation temperature, and the cell contains condensable vapor. Conversely, it is deactivated when these physical conditions are not met. By providing the derivative of the source term with respect to the dependent variable, the diagonal dominance of the discretized matrix was enhanced. Furthermore, the under-relaxation factors for momentum and energy equations were reduced to 0.3 and 0.5, respectively, to dampen drastic oscillations during the initial condensation phase. A rigorous time-step sensitivity analysis was conducted. Given the complex gas–liquid interfacial dynamics and the fine mesh required for the porous domain, the Courant–Friedrichs–Lewy (CFL) condition dictates a strict time-step restriction. We evaluated three distinct time steps: 10^{-5}, $0.5*10^{-5}$, and 10^{-6} *s*. The results indicated that time steps larger than 10^{-6} *s* led to non-physical velocity spikes and mass imbalance, whereas 10^{-5} *s* ensured that the global Courant number remained below 0.25, yielding stable and time-step-independent results.

It is important that simulating stability is achieved when time steps go beyond *2500*; thus, we selected numerical data when numerical stability was reached. To save computational time, the boundary conditions of the physical model were set as symmetric boundary conditions by *GAMBIT 2.4.6*. Grid refinement was applied to the near-wall regions. The total number of cells was *28000, 49500*, and *80410* respectively. Additionally, grid independence was checked before the calculations. All the operational conditions and geometric conditions are listed in *Table 4*.

Table 4. Operational and geometric conditions.

Parameters	Basic value	Range
Velocity of gas mixture (m/s)	0.3, 0.5, 1, 1.8, 2.8	0.3~2.8
T_{in} (K)	362.17	NA
T_{cool} (K)	293, 302, 313, 323	293~323
Length of ceramic tube (mm)	600	NA
Inner diameter of ceramic tube (mm)	12.04	NA
Thickness of membrane (mm)	1.5	NA
Mean diameter of pores in membrane (nm）	20	NA
Porosity	40%	NA
Tortuosity	2.084	NA
Vapor mass fraction	7.5%, 9%, 12%, 16%, 20%	7.5%~20%
Saturated pressure (Mpa)	0.103, 0.131	0.103~0.131
Saturated temperature (K)	315.29, 336.17	315.29~336.17

3. Results and Discussion

3.1. Model Validation and Grid Independence

Grid independence was checked before the calculations; when the grid number reached *80410*, it had a minor effect on the results of the numerical simulation. Additionally, grid refinement was applied to the near-wall regions. In order to validate the solution of the numerical simulation, a comparison between experimental and numerical results was conducted under the operational conditions shown in *Table 3*, and details are presented in *Figures 6*, *7*.

 doi:10.20944/preprints202603.2439.v1

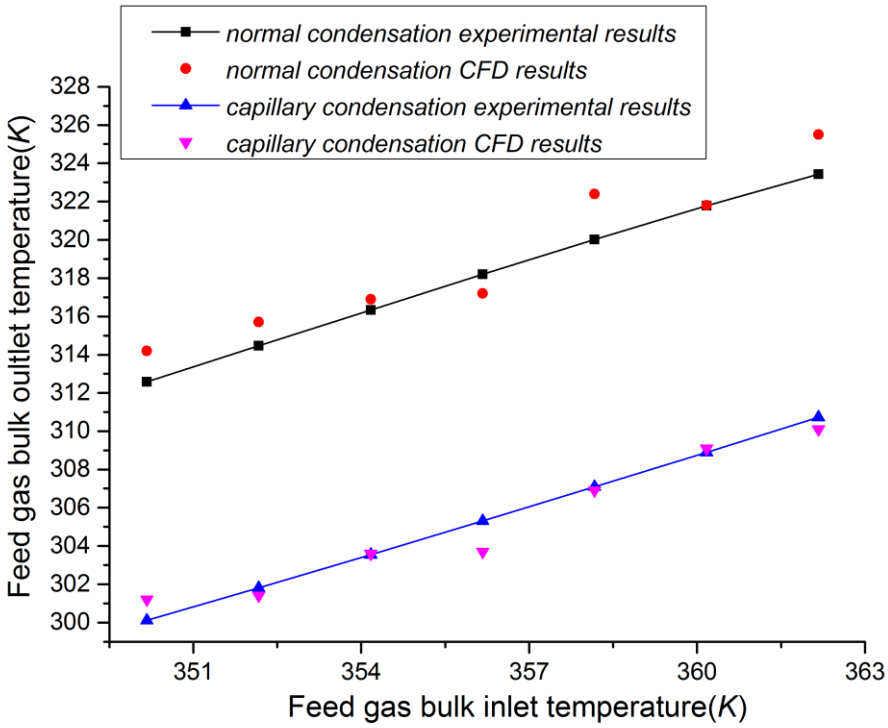

Figure 6. Comparison between the experimental and numerical results from the simulation (U_{in}=2.8m/s; t=1.5E-2s; $W_{vap,0}$=7.5%).

The variation in outlet feed gas bulk temperature ($T_{b,out}$) with different inlet feed gas bulk temperature ($T_{b,in}$) during normal condensation (NCD) and capillary condensation (CCD) processes is shown in *Figure 5*, where two curves and the scattered points represent the numerical simulation and experimental data, respectively. The variation trend of the numerical simulation data was similar with that of the experimental data; the maximum and minimum error between them was *1.14%* and *0.59%*, respectively. The change in condensation rate was also researched in NCD and CCD but without comparing $T_{b,out}$. The main panel in *Figure 7* reports the comparison of condensation rate in NCD between experimental (red dots) and numerical results (black line), while the insert in *Figure 7* is used to verify the accuracy of condensation rate in CCD. As can be seen from the figure, the errors between CFD and experimental results were in the range of *3.8%~4.6%*; therefore, the CFD data was reliable. Regarding the error analysis, a higher deviation in CCD mass flux (3.8%–4.6%) compared to bulk temperature is expected due to the complexity of the phase change process. While the Knudsen/viscous flow model (Equation 2) captures the dominant transport mechanisms, it assumes an idealized porous structure. In reality, micro-scale phenomena such as partial pore blocking by the condensate or non-uniform pore distribution may occur, which are challenging to fully resolve in a macroscopic CFD model. These factors affect mass transfer more significantly than bulk heat transfer, leading to the observed difference in accuracy. Nevertheless, the results remain well within the acceptable margin for engineering applications.

 doi:10.20944/preprints202603.2439.v1

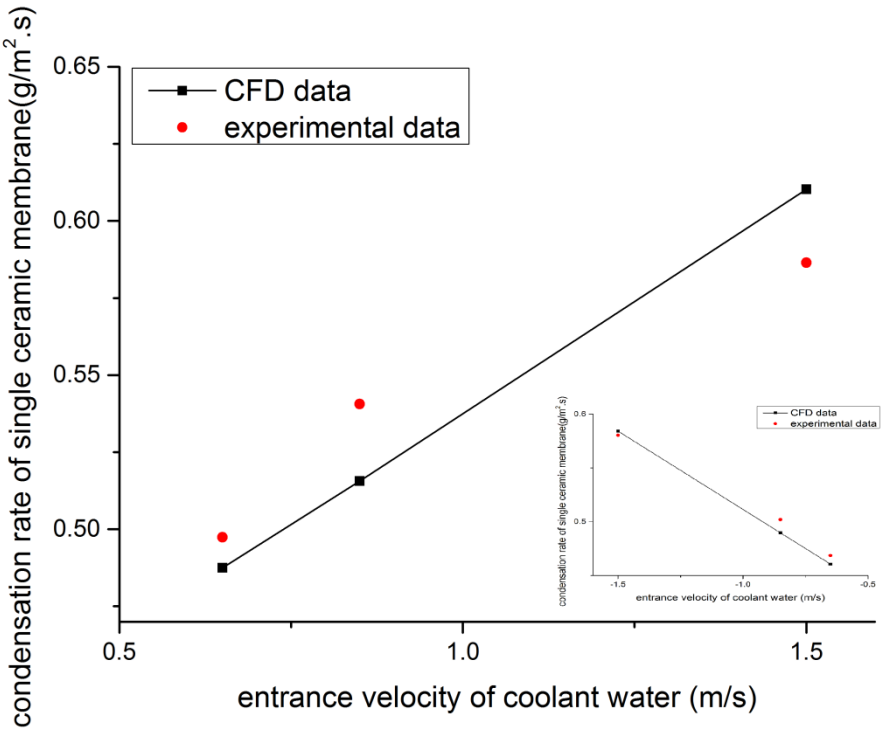

Figure 7. Comparison between the experimental and numerical results from the simulation (U_{in}=2.8m/s; t=1.5E-2s; $W_{vap,0}$=7.5%).

3.2. *Effects of Inlet Velocity on Two Types of Condensation*

In this part, the effects of feed gas inlet velocity (U_{in}) on two types of condensation processes were researched by analyzing the results of the experiment and the numerical simulation, respectively. In the experiment, the temperature difference of feed gas (ΔT_b) between the inlet and outlet and the mass flux of water recovery (m_{re}) were measured. Moreover, we analyzed the change in vapor mass fraction (W_{vap}) and radial velocity (U_r) using CFD. The experimental operational conditions were in accordance with those in CFD, where the initial parameters of vapor mass fraction ($W_{vap,0}$), inlet temperature (T_{in}), and the temperature of coolant water (T_{cool}) for NCD and CCD were set or controlled as *20%*, *293K*, and *362.17K* (NCD) or *323K* (CCD), respectively.

In order to achieve accurate results, every group of experiments was carried out five times under the same operational conditions, and the experimental data is presented in *Figures 8-11*. It is shown that the values of ΔT_b in NCD increased dramatically when U_{in} changed from *0.3* to *1.8m/s*, but they leveled off when U_{in} became larger than *1.8m/s*. The values of ΔT_b in CCD, however, declined linearly with an increase in U_{in}, as depicted in *Figure 9*; i.e., the influence of velocity on the thermal performance of NCD is totally opposite to that of CCD. The numerical model in this research was fitted with current operating conditions during the numerical simulation.

 doi:10.20944/preprints202603.2439.v1

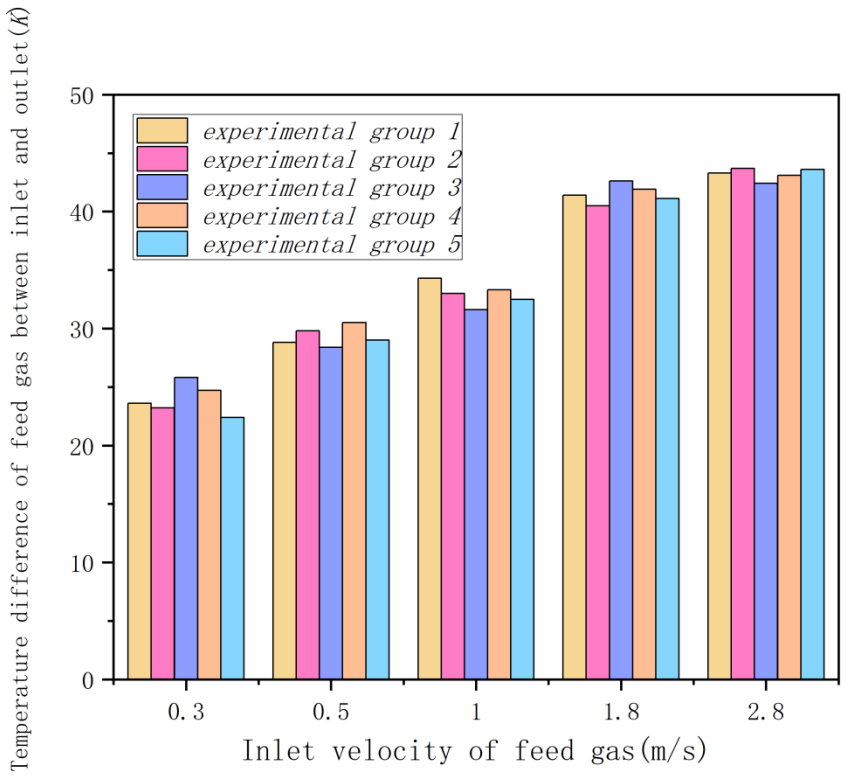

Figure 8. Variation in ΔT_b with different U_{in} in normal condensation (T_{in}=362.17K; T_{cool}=293K; $W_{vap,o}$=20%; *time=10mins*).

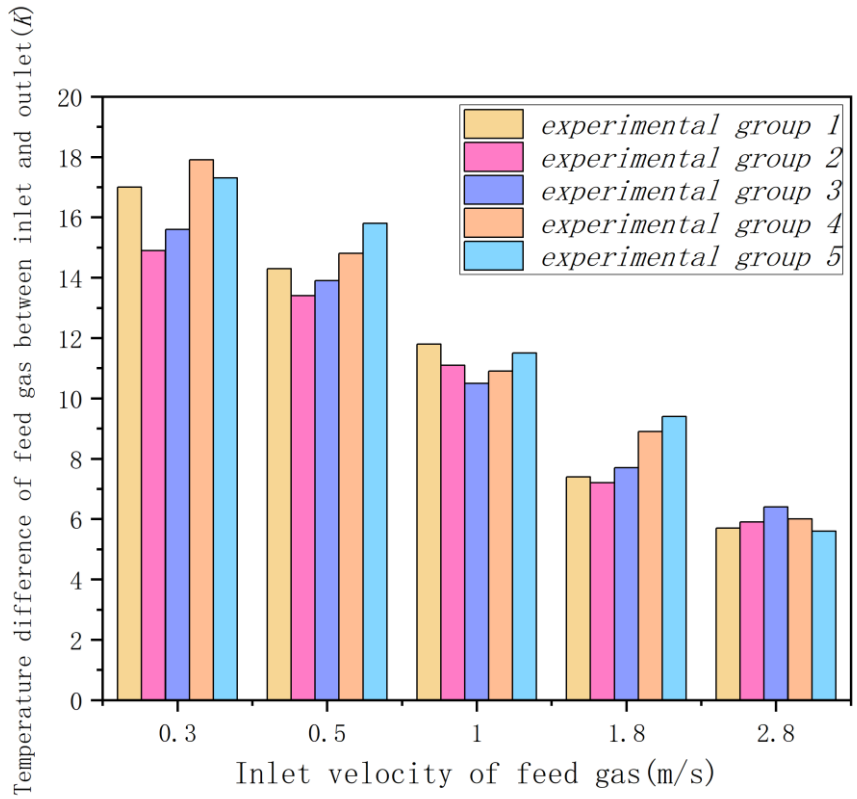

Figure 9. Variation in ΔT_b with different U_{in} in capillary condensation (T_{in}=362.17K; T_{cool}=323K; $W_{vap,o}$=20%; *time=10mins*).

 doi:10.20944/preprints202603.2439.v1

Additionally, we measured m_{re} (mass flux of water recovery) during the NCD and CCD processes. As shown in *Figure 10*, the values of m_{re} in NCD were enhanced with an increase in U_{in}, and the maximum and minimum values of m_{re} were *0.249* and *1.47kg/m².h*. Nevertheless, the values of m_{re} in CCD decreased with increasing U_{in} *(0.3* to *2.8m/s)*, as depicted in *Figure 11*. Compared with CCD, the ceramic membrane tube exhibited a distinct performance of heat and mass transfer at similar U_{in} when NCD occurred. This is primarily because normal condensation was relevant to heat transfer processes such as convection heat transfer and thermal conduction, which were significantly promoted by the high velocity of feed gas. During the capillary condensation process, however, the higher velocity would distort the boundary layer and hinder the performance of the ceramic membrane tube. Moreover, the water recovery amount was negative when the feed gas velocity was larger than *1m/s*, which also meant that capillary condensation was not able to develop efficiently at comparatively higher inlet velocity (U_{in}*>1m/s*). The negative recovery rate can be explained by the fact that most condensate layers were attached to the membrane surface due to surface tension and wetting characteristics, and the water uptake capacity also causes the condensate to stagnate within porous zones instead of being recovered timely.

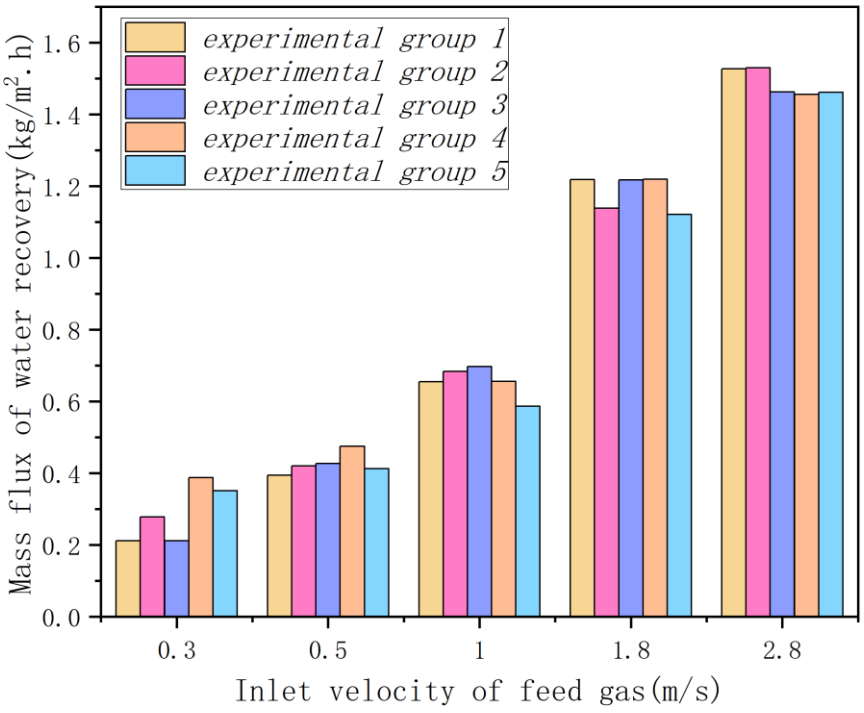

Figure 10. Variation in m_{re} with different U_{in} in normal condensation (T_{in}*=362.17K;* T_{cool}*=293K;* $W_{vap,0}$=20%; *time=10mins*).

 doi:10.20944/preprints202603.2439.v1

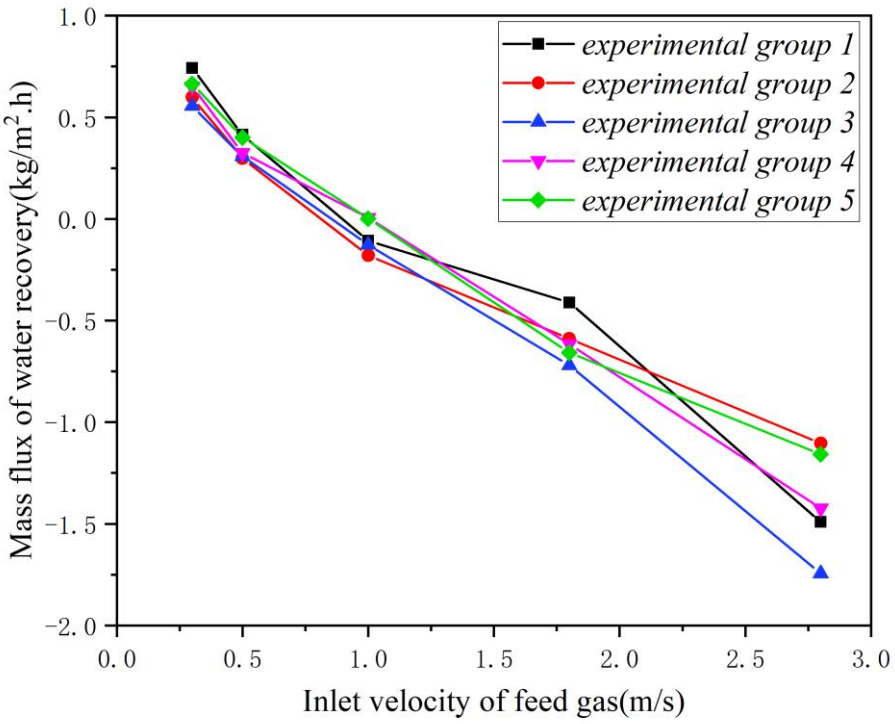

Figure 11. Variation in m_{re} with different U_{in} in capillary condensation (T_{in}=362.17K; T_{cool}=323K; $W_{vap,0}$=20%; *time=10mins*).

In the numerical simulation, we researched both the thermal and water recovery performance in the ceramic membrane tube with different inlet velocity (U_{in}). We took a section from every *100mm* in the tubular ceramic membrane, as mentioned above and as shown in *Figure 11, 12*. *Figure 11* shows the mass fraction of vapor (W_{vap}) distribution along the membrane tube versus U_{in} at fixed conditions during NCD. As the flow developed, the values of W_{vap} declined dramatically from the inlet (*x=0*). When the distance was larger than certain values (*x=400*), W_{vap} leveled off' i.e. the normal condensation proceeded more predominantly in the front of the ceramic membrane tube (*0~400mm*) compared to its back (*400~600mm*).

The change in mass fraction of water vapor (W_{vap}) could reflect the developing degree of capillary condensation (CCD); thus, we analyzed the variation in W_{vap} during the CCD process when U_{in} was *0.3, 0.5,* and *1m/s*. As shown in *Figure 12*, the variation in W_{vap} exhibited a nonlinear relationship with the *x-coordinate* in normal condensation. When the values of the *x-coordinate* changed from *0* to *450mm*, W_{vap} barely changed. Nevertheless, when the *x-coordinate* was over *450mm*, W_{vap} declined rapidly. Moreover, it was apparent that W_{vap} gradually increased as U_{in} increased (from *0.3m/s* to *1m/s*). Unlike in normal condensation, the mass fraction of water vapor only changed remarkably in the back of the ceramic membrane tube (*400~600mm*).

 doi:10.20944/preprints202603.2439.v1

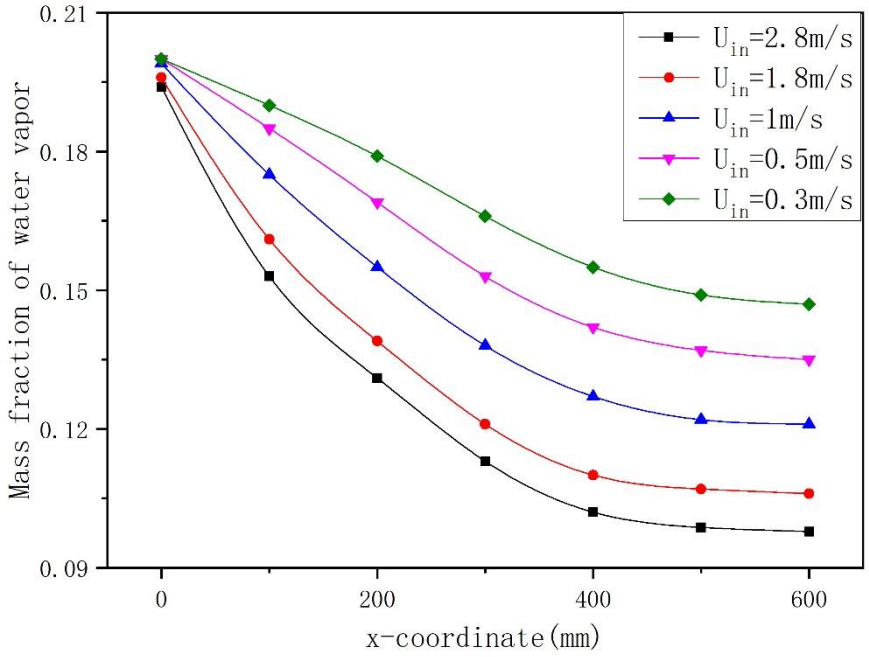

Figure 12. Variation in Wvap with different Uin in normal condensation (Tin=362.17K; Tcool=293K; Wvap,0=20%).

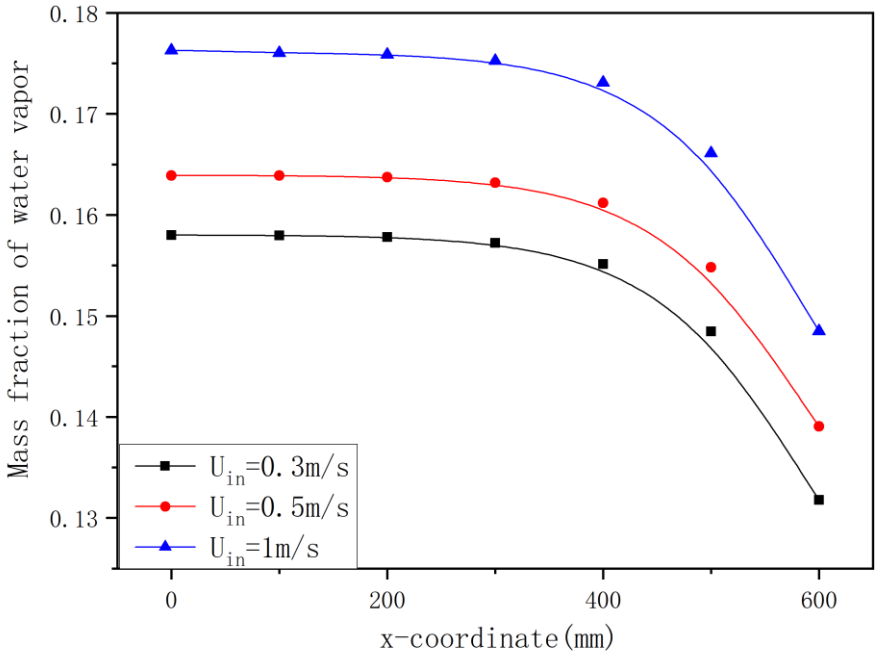

Figure 13. Variation in W_{vap} with different U_{in} in capillary condensation (T_{in}=362.17K; T_{cool}=323K; $W_{vap,0}$=20%).

According to the analysis of J.Li[17], non-condensable gas could accumulate in the near-wall region of ceramic membrane tubes, and this behavior would constrain the water vapor to condense into liquid. In addition, the radial velocity of feed gas (U_r) had apparent influence on the non-

 doi:10.20944/preprints202603.2439.v1

condensable gas, especially at higher U_r. With increasing U_r, the accumulated non-condensable gas became distorted, and the condensation process was able to occur.

Figure 14 shows the change in U_r with different U_{in} during the NCD and CCD processes, respectively. U_r was directed radially inward (-) when it was opposite to the direction of gravity. As presented in *Figure 14*, all the curves showed a similar variation tendency; the absolute values of U_r declined dramatically from the inlet of the membrane tube and then leveled off up to its outlet. As seen in *Figure 15*, the absolute values of U_r were almost zero for some distance from the inlet. Nevertheless, as the x-coordinate approached *500mm*, the absolute values of U_r increased rapidly (from *0* to *0.08m/s*).

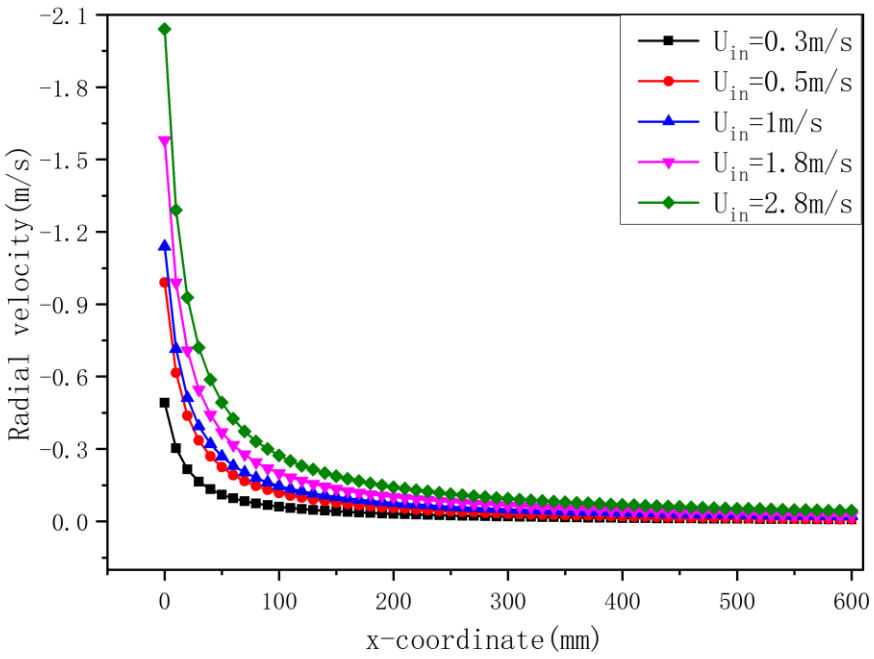

Figure 14. Variation in Ur with different Uin in normal condensation (Tin=362.17K; Tcool=293K; Wvap,0=20%).

The fluctuation depicted in the figure may be because the condensate adhering on the membrane wall is divided by three kinds of flow patterns: a flow pattern with a significant condensation heat and mass-transfer degree appearing in the front, one with an alleviating degree appearing in the middle, and one with a lower degree appearing in the back of the ceramic membrane. A similar conclusion was presented by Xie et al.[22], who found that the thermophoretic force pressed the condensate film onto the wall surface and the inertia force caused it to detach from the wall surface.

It can be concluded that the boundary layer would be squeezed as U_r increases, and both normal condensation (NCD) and capillary condensation (CCD) could proceed more efficiently. Therefore, NCD occurred significantly in the front of the TCM and slowed down gradually. However, CCD only appeared in the back of the TCM (the x-coordinate was larger than *500mm*).

3.3. Effects of W_{non} on Two Types of Condensation

The suction effect induced by non-condensable gas played an important role in thermal characteristics[11,17,19]. The fluid force balance in the pores within the nanoporous membrane can be obtained by considering capillary force (F_{ca}) and friction (f) in *Eq(25)*, *(26)*, respectively, therefore yielding *Eq(27)*:

$$F_{ca} = (d_{pore} + 2\delta)\sigma\cos\theta \tag{25}$$

 doi:10.20944/preprints202603.2439.v1

$$f = 8\pi\mu x \frac{dx}{dt} \tag{26}$$

$$\int_0^{t_1} (d_{pore} + 2\delta)\sigma \cos\theta dt = \int_0^{\delta} 8\pi\mu x dt \tag{27}$$

where δ , t, σ, θ, and d_{pore} represent the thickness of the TCM wall, time steps, surface tension, contact angle, and the diameter of pores within the TCM, respectively, and are listed in *Table 1*. The value of equilibrium time (t_1) equaled 2.52×10^{-4} and was obtained from *Eq(27)*; in other words, the fluid in the pores within the nanoporous membrane was in an equilibrium state of force when the simulation period was larger than $t_1(2.52\times10^{-4})$. The operation parameters analyzed were the vapor mass fraction (W_{vap}), the inlet bulk temperature of feed gas (T_{in}), and the average suction effect coefficient (φ_a).

More than the suction effect, the existence of non-condensable gases would change the partial pressure of water vapor, and consequently the condensation process would be slowed down. The predominant occurrence of CCD in the downstream section can be attributed to the synergistic effects of velocity decay and pressure distribution. As the fluid travels downstream, the pressure drop alters the local thermodynamic state, while the concurrent velocity decay increases the residence time of the vapor species. At the pore scale, this prolonged residence time under favorable pressure conditions facilitates capillary condensation according to the Kelvin equation, leading to the observed downstream deposition. Because of the accumulation of condensation droplets, a short condensation section is attached onto the micropore wall and maintains the flow state. The attaching principle for condensates on membrane wall surfaces is essentially governed by synergistic effects between the capillary force and the viscosity force. Consequently, the condensate liquid tends to accumulate in the downstream section of the membrane, especially in the primary stage.

Figure 16 presents the variation in W_{vap} for different W_{non} when T_{in}=362.17K, T_m=293K, U_{in}=1.8m/s, and $W_{vap,0}$ was *7.5%*, *9%*, *12%*, *16%*, and *20%*, respectively. In *Figures 15, 16*, the left and right side of the contours represent the inlet and outlet of the ceramic membrane, respectively. Furthermore, the blue zones represent the vapor condensed into liquid, and the red zones represent the feed gas; the other zones represent the gradual process of condensation. The non-condensable gas mass fraction (W_{con}) was calculated using *Eq(28)*:

$$W_{con} = 1 - W_{vap} \tag{28}$$

Consequently, $W_{con,0}$ was *92.5%*, *91%*, *88%*, *84%*, and *80%* in *Figure 15*.

Due to the efficiency of water recovery in capillary condensation (CCD) being relatively low, we just selected *2%*, *16%*, and *20%* as the values of W_{vap}. As shown in *Figure 16*, CCD only happened in the back of the ceramic membrane tube, which was consistent with the results in *Section 3.2* of this paper.

In both the NCD and CCD processes, the phase-transition regions (blue zones) became longer with the decrease in non-condensable gas mass fraction (W_{non}) at a fixed time. In order to account for this trend, it could be said that the suction effect and thermal resistance effect caused by non-condensable gas were more pronounced at higher W_{con}, which was in accordance with the results in this research[13]. Additionally, the whole membrane tube was filled with phase-transition regions during the NCD process, while phase-transition regions only occurred in its back during the CCD process. This also explains why the m_{re} of NCD was *1.2~3* times larger than that of CCD at fixed conditions.

 doi:10.20944/preprints202603.2439.v1

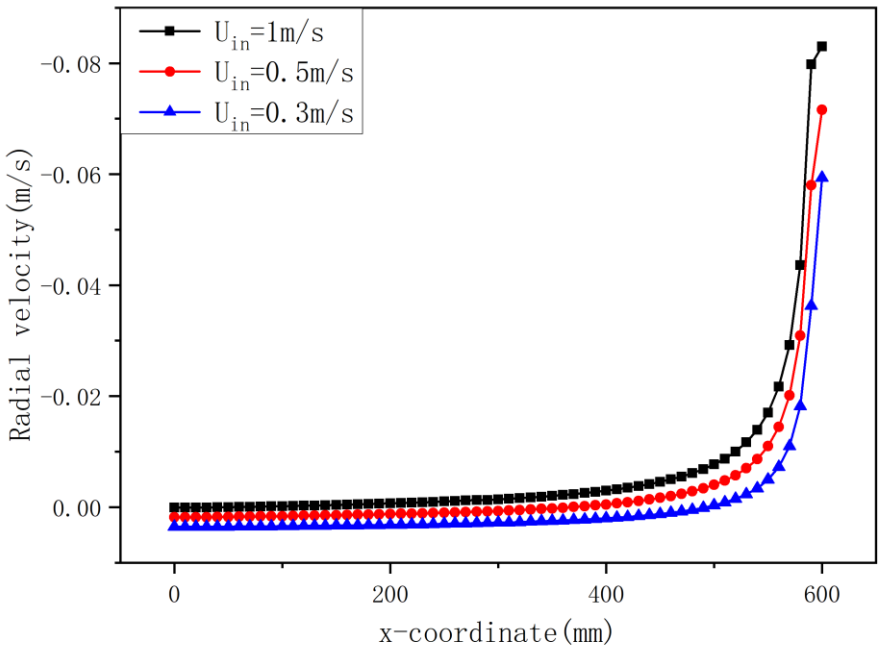

Figure 15. Variation in Ur with different Uin in capillary condensation (Tin=362.17K; Tcool=323K; Wvap,0=20%).

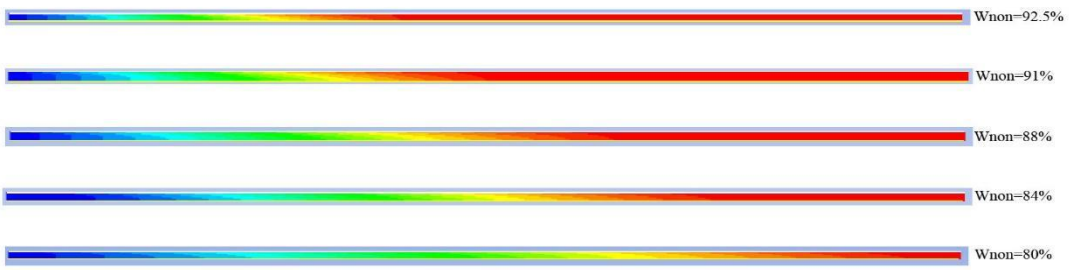

Figure 16. Contours of water vapor with different W_{vap} in normal condensation (T_{in}=362.17K; T_{cool}=293K; U_{in}=1.8m/s; t=3.2s).

Figure 17. Contours of water vapor with different W_{vap} in capillary condensation (T_{in}=362.17K; T_{cool}=323K; U_{in}=0.3m/s; t=3.2s).

According to G.Caruso et al.[12], the suction effect coefficient φ, in a molar approach, was:

$$\varphi = \frac{1}{\delta}\ln\left(\frac{1-W_{vap}}{1-W_{vap,0}}\right) = \frac{1}{\delta}\ln\frac{W_{non}}{W_{non,0}} \tag{29}$$

Figure 18 shows the variation in average suction effect coefficient (φ_a) with the increment of W_{vap}, where φ_a represents the average value of the suction effect coefficient during the flow. The results show a similar trend for different time steps (t) in which the highest and lowest values of φ_a occurred

 doi:10.20944/preprints202603.2439.v1

at W_{vap}=7.5% and W_{vap}=20%, respectively. This finding could be attributed to the fact that for each time step (t), the higher the value of W_{vap}, the lower the value of φ_a in the membrane. Additionally, φ_a declined dramatically with the passage of time. It could be further seen that the experimental proceeding time had a minor effect on φ_a at larger W_{vap}, such as 20%.

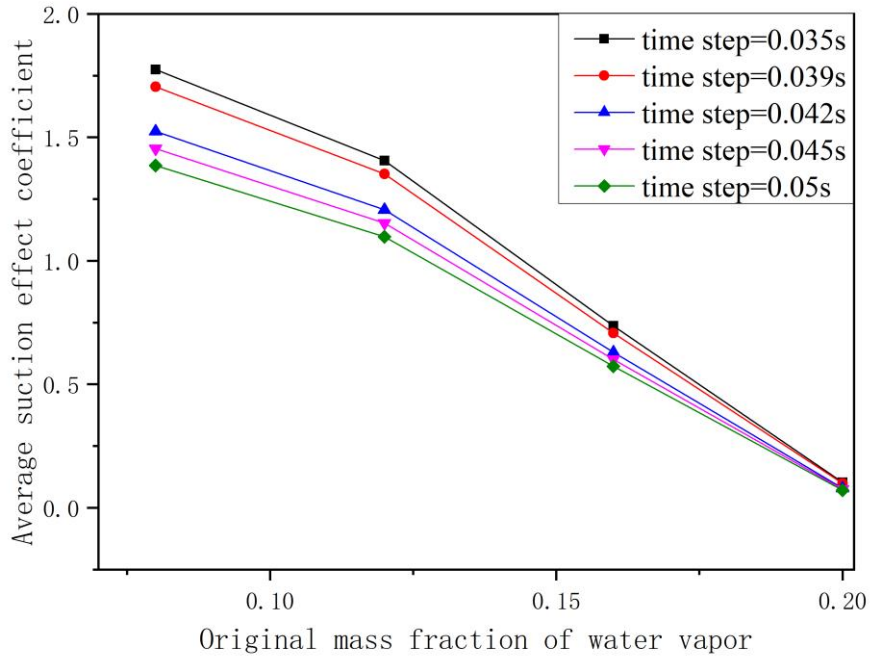

Figure 18. φ_a distribution along the W_{vap} versus time (T_{in}=371.63 K; T_{cool}=293K; U_{in}=1.8m/s).

3.4. Effect of T_{cool} on Normal Condensation

Because the maximum T_{cool} heated by the electric heater (*No.7* in the experimental module) was *323K* and the T_{sat} was *315.29K* at a fixed operational pressure, in order to guarantee that T_{cool} was always larger than T_{sat} when researching the capillary condensation, the variable range of T_{cool} was very limited. As a result, we only analyzed normal condensation in this part.

The condensation heat flux (q_{con}) and condensation mass flux (m_{con}) generated in the near-wall region can be calculated by *Eq(30),(31)*:

$$q_{con} = h(T_b - T_{wall}) \tag{30}$$

$$m_{con} = \frac{q_{con}}{\gamma} \tag{31}$$

where h and γ represent the convective heat transfer coefficient and latent heat, respectively.

The numerical data is shown in the following figures. The curves presented in *Figures 19* and *20* changed dramatically in the initial stage and then declined gradually until the end. Because the material of the membrane tube wall surface was hydrophilic, the phase transition on it could regarded as film-wise condensation, and the convective heat flux was relatively high. In addition, the values of q_c and m_{con} were enhanced with the decrease in T_{cool} due to the fact that the heat transfer process was sensitive to the temperature difference between the feed gas and coolant water.

 doi:10.20944/preprints202603.2439.v1

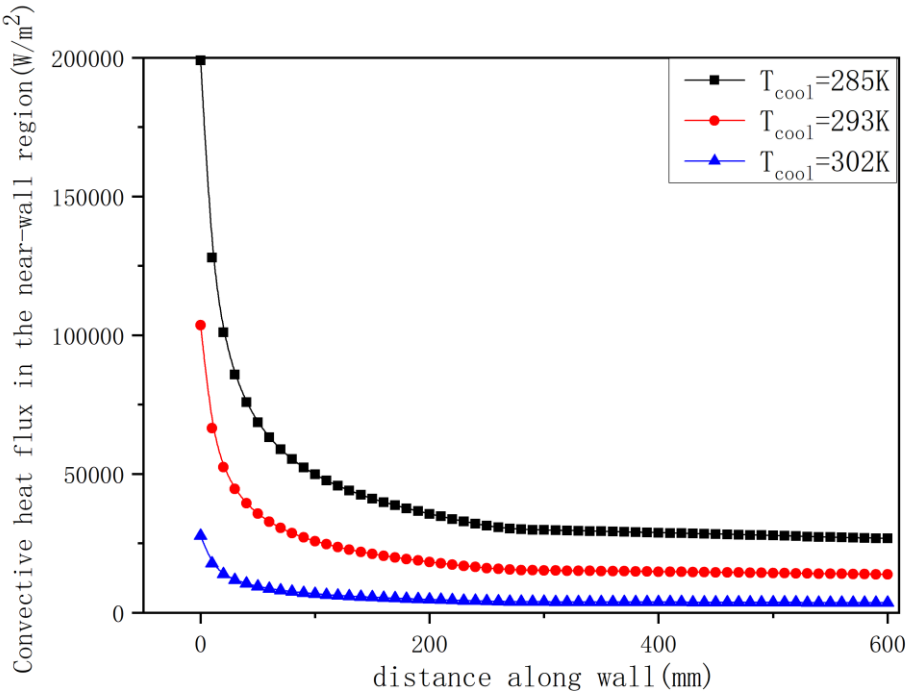

Figure 19. qc distribution along the ceramic tube versus Tcool (Tin=371.63 K; Uin=1.8m/s; t=3.2s).

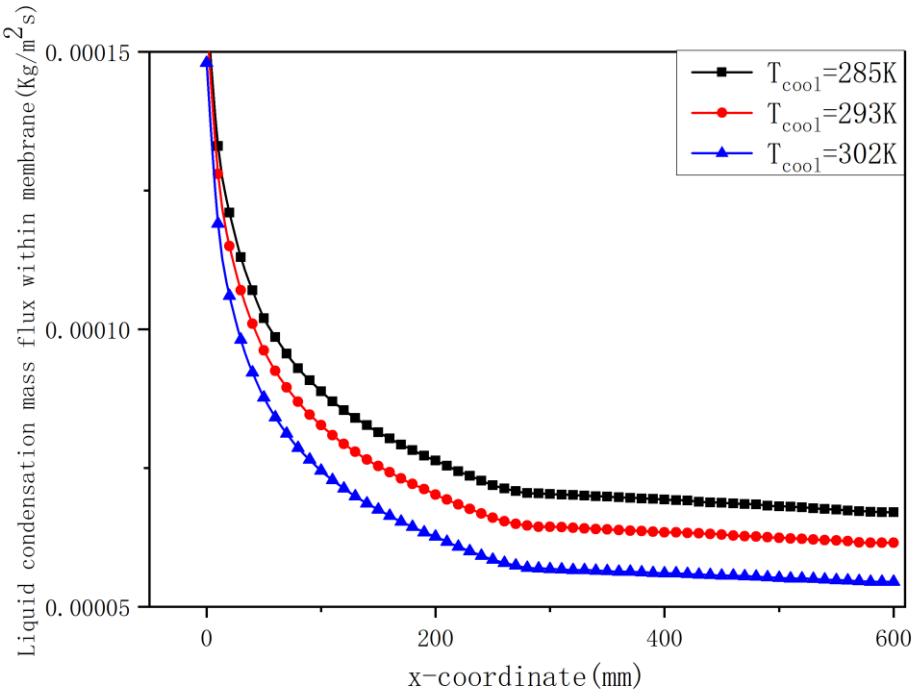

Figure 20. m_{con} distribution along the ceramic tube versus T_{cool} (T_{in}=371.63 K; U_{in}=1.8m/s; t=3.2s).

Figure 21 shows the convective heat transfer coefficient (h) distribution along the *y-coordinate* for different T_{cool}, where *y=600mm* represents the membrane wall surface (as depicted in *Figure 1*). As depicted in *Figure 21*, the forced convective heat transfer proceeded significantly in the near-wall region of the membrane tube. Furthermore, the variation tendencies of h along the *y-coordinate* for varied T_{cool} were completely different. At a fixed x-coordinate, h declined dramatically with increasing

 doi:10.20944/preprints202603.2439.v1

T_{cool}, which was indicative of the fact that the forced convective heat transfer process was sensitive to the temperature difference between the feed gas and cooling water.

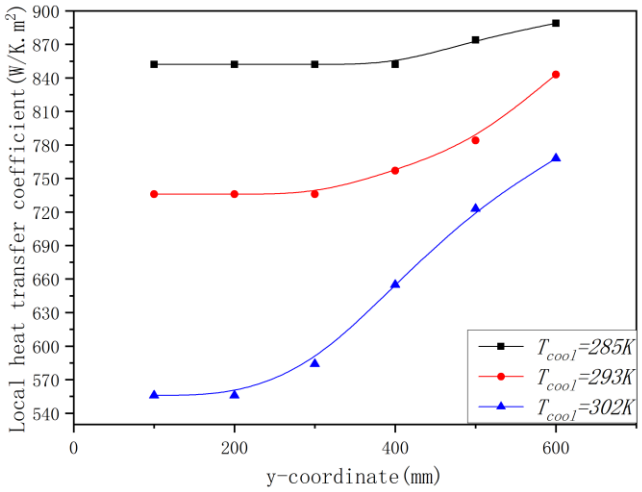

Figure 21. *h* distribution along the ceramic tube versus T_{cool} (T_{in}=371.63 K; U_{in}=1.8m/s; *time=10mins*).

According to the results from the observational experiment, we also analyzed the variation in weight of water recovery (m'_{re}) with different T_{cool} in *five* groups experimentally, and present the data in *Figure 22*. The results show a declining trend in which the highest and lowest m'_{re} occurred at T_{cool}=*285K* and T_{cool}=*302K*, respectively. When T_{cool} increased from *285K* to *302K*, m'_{re} with other conditions fixed increased by approximately *3.5* times. Typically, the thickness of the condensate film apparently increases with experimental time, and the maximum thickness reaches *6.63 mm* after *60 s*. This is because the multi-level condensation process is influenced by the distribution of condensate droplets and condensate films. Condensate morphology also reflects the intensity of the condensation heat and mass transfer process.

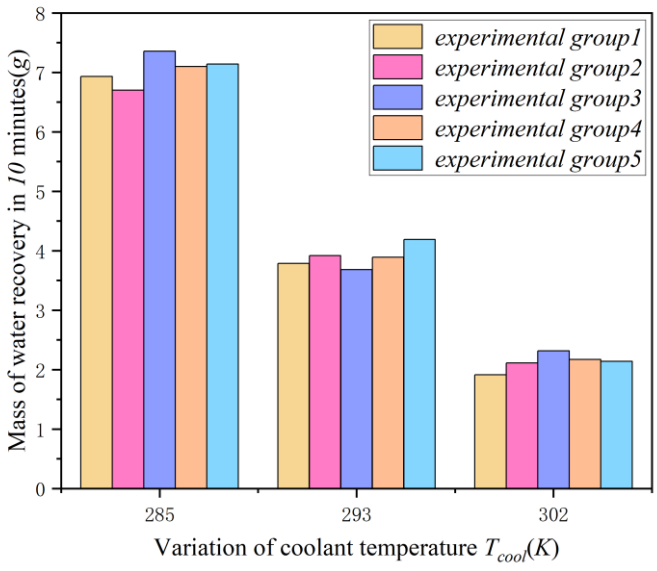

Figure 22. m're distribution along the ceramic tube versus Tcool (Tin=371.63 K; Uin=1.8m/s; time=10mins).

 doi:10.20944/preprints202603.2439.v1

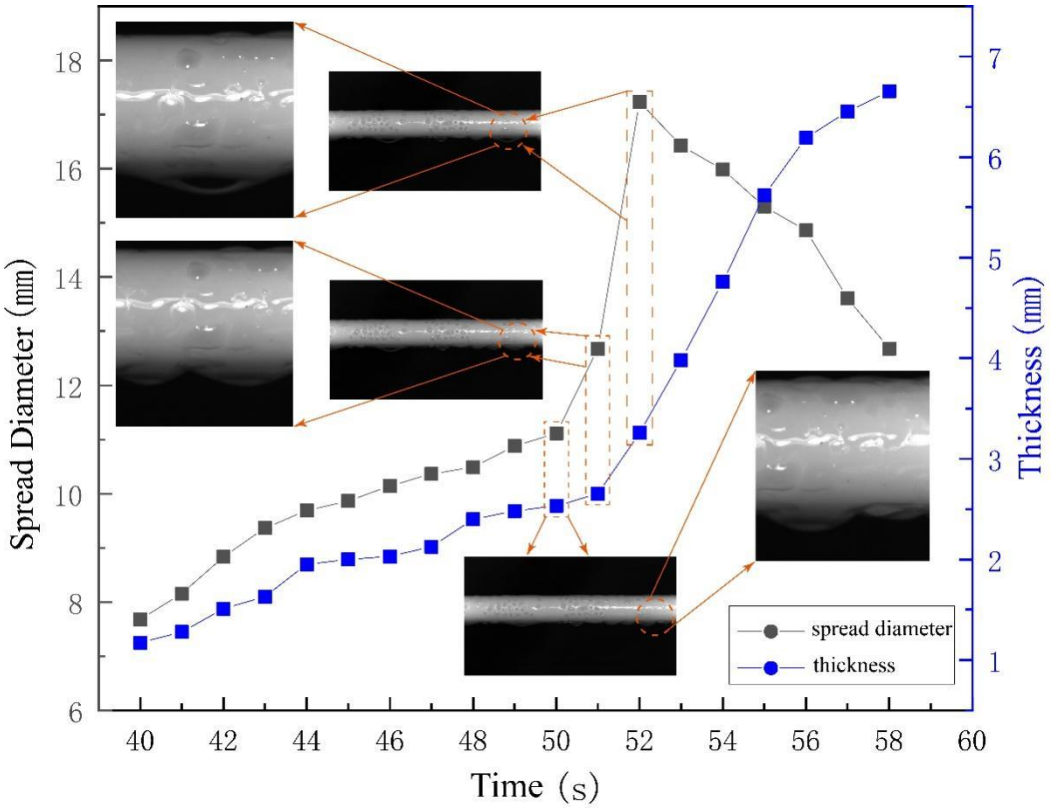

Figure 23. m'_{re} distribution along the ceramic tube versus T_{cool} (T_{in}=371.63 K; U_{in}=1.8m/s; *time=10mins*).

4. Conclusion

The thermal and mass transfer performance of the tubular transport membrane condenser (TCM) was systematically investigated through both numerical and experimental approaches. By analyzing the coupled effects of operational parameters—including inlet velocity, cooling water temperature, and non-condensable gas mass fraction—the main findings are as follows.

The developed numerical model demonstrated excellent agreement with the experimental data. The maximum relative errors were strictly controlled within *1.14%* and *0.59%* for the normal condensation (NCD) and capillary condensation (CCD) processes, respectively, ensuring high reliability for the flow and heat transfer predictions.

The NCD process occurred uniformly across the entire tube length. During this process, both the water recovery rate and the bulk temperature difference increased monotonically with inlet velocity (from *0.3* to *2.8 m/s*), peaking at *1.47 kg/(m²·h)* and *42.7 K*, respectively. Conversely, the CCD process was predominantly localized in the downstream region (*x=450–600 mm*) due to the synergistic effects of pressure drop and velocity decay. Notably, CCD became highly inefficient for water recovery when the inlet velocity exceeded *1.0 m/s*.

The impact of non-condensable gases was quantified using the average suction effect coefficient (φ_a). Both numerical and experimental results confirmed that a lower non-condensable gas mass fraction directly yields a reduced φ_a within the TCM. Furthermore, φ_a exhibited a sharp decline over time, although the experimental duration had a negligible impact when the initial vapor mass fraction was maintained at *20%*.

The multi-stage condensation performance was highly sensitive to the cooling water temperature. Decreasing the cooling temperature from *302 K* to *285 K* led to an approximate *3.5*-fold increase in the water recovery mass under constant operating conditions, underscoring the strong dependence of mass transfer on local thermal gradients.

Consequently, this fundamental exploration of two-phase flow characteristics and heat transport mechanisms during multi-stage condensation on porous surfaces provides critical insights for

 doi:10.20944/preprints202603.2439.v1

optimizing tubular TCMs. These findings pave the way for more efficient designs in industrial water harvesting and waste heat recovery, contributing broadly to global energy conservation and carbon reduction initiatives.

Acknowledgments: The authors are grateful for the support of "Key Projects of Jilin Province Science and Technology Development Plan" (grant no. 20250801123FG).

Nomenclature

Notations	**Subscripts**
λ: thermal conductivity (W/m.K)	*mass*: mass conservation equation
h: convective heat transfer coefficient ($W/K.m^2$)	*vap*: vapor
p: static pressure (Pa)	*non*: non-condensable gas
T: temperature (K)	*sat*: saturated state of flow
V: velocity vector	*pore*: the pores within the membrane
U: velocity magnitude (m/s)	*per*: permeation mass flux
R: specific gas constant	*m*: ceramic membrane tube
d: diameter (m)	*con*: condensation
A: area (m^2)	*re*: mass flux of water recovery
v': volume (m^3)	*all*: overall
q: heat flux (kJ/m^{2}s)	*species*: species conservation equation
D: diffusion coefficient (m^2/s)	*enr*: energy conservation equation
t: time step (s)	*r*: radial
M: molar weight (kg/mol)	*b*: bulk of feed gas
m: mass flux (kg/m^2.s)	*cool*: cooling water
m': weight (g)	*mom*: momentum
J: diffusion mass flux (kg/m^2.s)	*0*: initial state
Kn: Knudsen number	*eff*: efficient diffusion coefficient
W: mass fraction	*ca*: capillary
f: friction (N)	*th*: thermophoretic force
F: force (N)	*i*: inertia force
x: distance along the ceramic tube (mm)	*cell*: cells in the near-wall region
k_B: Boltzmann constant	*in*: inlet of membrane module
k_0: permeability coefficient	*out*: outlet of membrane module
C_m,C_t,C_s: constant numbers	
Greek letters	
ρ: density (kg/m^3)	δ: thickness (m)
μ: dynamic viscosity (Pa.s)	γ: latent heat (KJ/Kg)
σ: characteristic size of the gas mixture (nm)	φ: suction effect coefficient
Ψ: porosity	θ: contact angle (^{o})

References

 doi:10.20944/preprints202603.2439.v1

1. P.E. Okafor, C.B. He, G.H. Tang, A critical review of superinsulation performance of ceramic nanofibrous aerogel for extreme conditions: Modeling, fabrication,applications, and outlook, Adv. Colloid Interf. Sci. 2025.335:p.103-352,
2. Zhou, Y., et al., Effect of mass transfer on heat transfer of microporous ceramic membranes for water recovery. International Journal of Heat and Mass Transfer, 2017. 112: p. 643-648.
3. Hu, H.W., G.H. Tang and D. Niu, Wettability modified nanoporous ceramic membrane for simultaneous residual heat and condensate recovery. Scientific Reports, 2016. 6(1).
4. R. Gulfam, T.E. Huang, C.X. Lv, et al., Condensation heat transfer on phase change slippery liquid-infused porous surfaces, Int. J. Heat Mass Transf.2022 185:p.122-384,
5. Uchytil, P. and T. Loimer, Large mass flux differences for opposite flow directions of a condensable gas through an asymmetric porous membrane. Journal of Membrane Science, 2014. 470: p. 451-457.
6. Loimer, T., Linearized description of the non-isothermal flow of a saturated vapor through a micro-porous membrane. Journal of Membrane Science, 2007. 301(1-2): p. 107-117.
7. Fu, W., et al., Numerical investigation of convective condensation with the presence of non-condensable gases in a vertical tube. Nuclear Engineering and Design, 2016. 297: p. 197-207.
8. Bao, A., D. Wang and C. Lin, Nanoporous membrane tube condensing heat transfer enhancement study. International Journal of Heat and Mass Transfer, 2015. 84: p. 456-462.
9. Hu, H.W., G.H. Tang and D. Niu, Wettability modified nanoporous ceramic membrane for simultaneous residual heat and condensate recovery. Scientific Reports, 2016. 6(1).
10. Asfand, F., Y. Stiriba and M. Bourouis, CFD simulation to investigate heat and mass transfer processes in a membrane-based absorber for water-LiBr absorption cooling systems. Energy, 2015. 91: p. 517-530.
11. Huang, J., J. Zhang and L. Wang, Review of vapor condensation heat and mass transfer in the presence of non-condensable gas. Applied Thermal Engineering, 2015. 89: p. 469-484.
12. Caruso, G. and D. Vitale Di Maio, Heat and mass transfer analogy applied to condensation in the presence of noncondensable gases inside inclined tubes. International Journal of Heat and Mass Transfer, 2014. 68: p. 401-414.
13. Yi, Q., et al., Visualization study of the influence of non-condensable gas on steam condensation heat transfer. Applied Thermal Engineering, 2016. 106: p. 13-21.
14. Behrang, A., et al., A theoretical study on the permeability of tight media; effects of slippage and condensation. Fuel, 2016. 181: p. 610-617.
15. Zschaeck, G., T. Frank and A.D. Burns, CFD modelling and validation of wall condensation in the presence of non-condensable gases. Nuclear Engineering and Design, 2014. 279: p. 137-146.
16. Wang, X., H. Chang and M. Corradini, A CFD study of wave influence on film steam condensation in the presence of non-condensable gas. Nuclear Engineering and Design, 2016. 305: p. 303-313.
17. Li, J., CFD simulation of water vapour condensation in the presence of non-condensable gas in vertical cylindrical condensers. International Journal of Heat and Mass Transfer, 2013. 57(2): p. 708-721.
18. Dehbi, A., F. Janasz and B. Bell, Prediction of steam condensation in the presence of noncondensable gases using a CFD-based approach. Nuclear Engineering and Design, 2013. 258: p. 199-210.
19. [19].Q. Xue, Y.J. Lim, R. Wang, Chemically robust hollow fiber thin-film composite membranes based on polyurea selective layers for nanofiltration under extreme pH conditions, J. Membr. Sci. 738 (2026) 124818.
20. G.S. Yao, J.L. Xu, Y.J. Feng, et al., Solar-driven interfacial evaporation of a hanging liquid marble, Sol. Energy Mater. Sol. Cells 2022:p.234.111-430.
21. W.H. Lei, M.R. Wang, X.K. Lu, et al., Reverse capillary trapping and self-removal of non-aqueous fluid from dead-end structures by nanoparticle suspension, J. FluidMech. 2025. 1009(A14).
22. J. Xie, Q.T. She, J.L. Xu, et al., Mixed dropwise-filmwise condensation heat transfer on biphilic surface, Int. J. Heat Mass Transf.2020:p.150.119-273.
23. Farber E M, Seraphim N M, Tamakuwala K, et al. Porous materials: The next frontier in energy technologies[J]. Science, 2025, 390(6772): eadn9391.
24. Li L, Sun X, Miao J, et al. Gradient engineering in interfacial evaporation for water, energy, and mineral harvesting[J/OL]. Energy & Environmental Science, 2025.

 doi:10.20944/preprints202603.2439.v1